The Astrophysical Journal Letters, 982:L48 (8pp), 2025 April 1 https://doi.org/10.3847/2041-8213/adbca3

Nonlinear and Nonmonotonic Effect of Ocean Tidal Mixing on Exoplanet Climates and Habitability

Maria Di Paolo[1], David P. Stevens[1], Manoj Joshi[2,3], and Rob A. Hall[2]
[1] Centre for Ocean and Atmospheric Sciences, School of Engineering, Mathematics and Physics, University of East Anglia, Norwich NR4 7TJ, UK; M.Di-Paolo@uea.ac.uk
[2] Centre for Ocean and Atmospheric Sciences, School of Environmental Sciences, University of East Anglia, Norwich NR4 7TJ, UK
[3] Climatic Research Unit, University of East Anglia, Norwich NR4 7TJ, UK
Received 2024 December 19; revised 2025 February 28; accepted 2025 March 1; published 2025 March 28

Abstract

Tides play an important role in the circulation and mean state of the Earth's oceans through inducing significant mixing. On other planets, tidal forcings could be highly amplified compared to Earth, such as planets orbiting relatively close to low-mass host stars, or planets having massive and/or close moons. The former scenario is especially important as, due to their abundance and their observational advantages, low-mass stars offer the best chance of finding habitable planets through sheer numbers. By varying the magnitude of tidal forcing over several orders of magnitude in a coupled atmosphere–ocean global circulation climate model, we find that key climatic quantities, such as heat transport intensity and both surface and deep ocean temperature, change with tidal strength in a nonlinear and nonmonotonic manner. We find an optimum value of tidal mixing, approximately 100 times that of Earth's oceans, which minimizes climatic thermal gradients across the planet. In particular, we show that such planets are habitable for stellar flux values at which oceans with weaker or stronger tidal mixing freeze globally, suggesting an important role for ocean tidal mixing in planetary habitability.

Unified Astronomy Thesaurus concepts: Exoplanets (498); Ocean tides (1152); Habitable planets (695); M stars (985); Planetary climates (2184); Ocean-atmosphere interactions (1150); Astrobiology (74); Exoplanet atmospheres (487); Planetary atmospheres (1244); Atmospheric circulation (112); Atmospheric dynamics (2300)

1. Introduction

The oceans on exoplanets remain largely unknown, as are the vast majority of precise exoplanetary characteristics, since only a few of them can be inferred from observational studies. The ocean on our planet has been extensively studied, and its importance in determining Earth's climate is well established. Earth's ocean is tightly coupled with the atmosphere and cryosphere, with which it exchanges considerable amounts of water, heat, and biogeochemical tracers. For instance, the poleward transport of energy from the tropics carried out by ocean circulation has a significant impact on our planet's climate, so much so that the magnitude of oceanic heat transport can be considered comparable to that of the atmospheric heat transport within the tropics (K. E. Trenberth & J. M. Caron 2001). Moreover, switching off ocean circulations and consequently their heat transport would cause an expansion of the sea ice coverage, with a drop in surface temperatures at high latitudes (M. Winton 2003). Our planet would experience more extreme geographic, seasonal, and diurnal variability in surface temperature, which could potentially render sizable areas uninhabitable for advanced forms of life (P. L. Read 2014). Given the key role of the ocean on Earth's climate and habitability, studies of exoplanetary oceans and their impact on climate are of great importance.

The vast majority of research focused on exoplanetary climate adopts atmospheric general circulation models (AGCMs) of varying degrees of complexity, often coupled to simplified models of the ocean, such as slab oceans with a depth of 50 m or 100 m, and often rely on prescribed heat fluxes. While this type of study is certainly worthwhile and leads to important results, the lack of coupling to a dynamic ocean precludes an accurate treatment of ocean circulation. Including ocean tides, ocean currents, heat transport, and sea ice (J. Cullum et al. 2014, 2016; Y. Hu & J. Yang 2014; S. L. Olson et al. 2020) can lead to significant qualitative differences in the results of exoclimate studies. More specifically, adopting a coupled atmosphere–ocean general circulation model (AOGCM) is particularly advisable when considering scenarios in which the consideration of ocean dynamics can have an important impact on climate.

Studies of habitability of planets orbiting cool stars, and more specifically M dwarfs, are especially interesting for several reasons. Not only are M dwarfs the most numerous stars in the solar neighborhood, offering the best chance of finding habitable planets through sheer numbers, but they also present evident observational advantages. Moreover, the longevity of M dwarfs represents a benefit for the chances of detecting potentially habitable planets, as these host stars provide a stable environment for the conditions required for the origin and the evolution of life (A. L. Shields et al. 2016).

The orbital distance of the circumstellar habitable zone around low-mass stars is significantly smaller compared to the case of solar-type stars, as a consequence of the lower luminosity of low-mass stars. Thus, planets orbiting low-mass stars are more strongly impacted by tidal interactions, causing frictional forces that result in torques that alter the planet's rotational angular momentum. Over time the tidal torques fix the rotation rate at a specific frequency: a process known as tidal locking. According to equilibrium tide theory (C. D. Murray & S. F. Dermott 1999), tidally locked planets on circular orbits are destined to rotate synchronously (the

periods for the completion of one rotation and one orbit around the central body become identical), always exposing the same face to the host star. However, due to a complex interplay of several factors, planets are not necessarily expected to be exact synchronous rotators, but rather to experience an imperfect tidal locking (see Section 2). We choose to investigate the case of an asynchronously rotating planet, therefore characterized by a traveling tide that moves across the planetary surface, consequently affecting ocean tidal-driven vertical mixing. It is well known that oceanic meridional overturning circulation and meridional heat transport have a dependence on vertical mixing (F. Bryan 1987; G. K. Vallis & R. Farneti 2009).

A few studies have investigated the role of ocean heat transport by using fully coupled AOGCMs to carry out exoplanet climate simulations. These publications provided a demonstration of the relevance of exooceanography in studying the climate of exoplanets and in determining their potential habitability (D. Ferreira et al. 2014; C. Kilic et al. 2018; A. D. Del Genio et al. 2019). However, to our knowledge, only one recent study investigated the process of tidal-driven vertical ocean mixing (Y. Si et al. 2022)—and that study assumed Earth-like continents and bathymetry. The authors investigated the effect of high vertical diffusivity (with a parameter 10 and 100 times greater than the one of the Earth) on the ocean circulation and surface climate of asynchronously rotating Earth analogs. They found that higher vertical diffusivity strengthened the meridional overturning circulation, enhancing heat transport from the tropics to high latitudes and resulting in overall surface warming.

We conduct studies using the coupled AOGCM FORTE2.0 (A. T. Blaker et al. 2021) to investigate the effects of tidal mixing on climate and habitability. Since the continental configuration of exoplanets cannot be currently constrained from observational studies, we use a custom continental "ridgeworld" configuration (see Section 2), which stops the formation of unrealistically large zonal jets in the ocean that typically occur in aquaplanet models, and allows the formation of ocean gyres, while being more general than assuming the specific continental configuration of present-day Earth.

As strong tidal interactions are tightly linked to the ocean vertical mixing (which we parameterize as a vertical diffusivity κ; R. Musgrave et al. 2022), we demonstrate how taking account of the impact of ocean tides can lead to significant effects on planetary climate. A higher ocean vertical diffusivity, associated with a stronger tidal forcing, is not intended to be necessarily due to the modeled planet orbiting a low-mass star, but can also be interpreted as linked to planets orbited by close and/or massive satellites. We intend to present a comparison of high diffusivity results and scenarios characterized by κ of the same order of magnitude of κ on Earth. In order to do so, we conduct an idealized study, focusing on varying a single parameter of the multidimensional parameter space. We vary the value of κ over a range of 4 orders of magnitude (see Section 2), which reveals nonlinear climatic effects and consequently a nonmonotonic impact on the position of the outer edge of the habitable zone.

2. Methods

2.1. Model Description

We adopt FORTE2.0 (A. T. Blaker et al. 2021), a fast and flexible intermediate-resolution coupled AOGCM. The ocean general circulation model Modular Ocean Model-Array Processor (MOMA; D. J. Webb 1996) is coupled to the atmospheric general circulation model Intermediate Global Circulation Model version 4 (IGCM4; M. Joshi et al. 2015). The ocean and atmosphere components of the model are coupled once per model day.

In the version of MOMA adopted here, the modeled ocean is characterized by a horizontal resolution of $2^\circ \times 2^\circ$ and by 15 z-layer levels, whose thickness increases progressively with depth, starting from 30 m at the surface and ending with a 836.10 m layer at the bottom. The ocean reaches a depth of about 5500m.

The configuration of the IGCM4 is characterized by a T42 spectral resolution, a grid spacing of approximately $2.^\circ 8$, and a troposphere-only atmosphere that extends to around 25 km altitude and is subdivided in 20σ levels.

2.2. Tidal Mixing Parameterization

Planets in close orbit around their host star experience particularly strong tidal interactions. Thus, potentially habitable planets orbiting M dwarfs are often tidally locked. However, under some circumstances (e.g., eccentricity, spin–orbit resonances, interactions in multiplanet systems) these planets may not be synchronously rotating (R. Barnes 2017). For instance, planets on eccentric orbits will not evolve to a state of synchronous rotation, but rather will rotate supersynchronously. For example, it is believed that an initially high orbital eccentricity of Mercury led to its capture into a 3:2 resonance (A. C. M. Correia & J. Laskar 2004). Furthermore, other phenomena can modify the rotational velocity of a planet and even counteract the effects of tidal damping. One example is given by the torque exerted by the Sun's gravitational field on Venus's atmospheric tide, which balances the despinning effect of tides raised in the body of the planet, resulting in its slow retrograde rotation (A. R. Dobrovolskis & A. P. Ingersoll 1980). Atmospheric tides have been shown to be a mechanism potentially capable of desynchronizing Earth-mass planets in the habitable zone of lower-mass stars with much sparser atmospheres than Venus (J. Leconte et al. 2015). Therefore, asynchronously rotating potentially habitable planets around M stars can be subjected to large traveling tides, and are therefore characterized by enhanced oceanic vertical mixing and diffusion.

In order to estimate the magnitude of vertical diffusivity, κ, we need to quantitatively determine the orbital radius of an exoplanet residing in the habitable zone of an M star. The M spectral class is divided into nine different groups, numbered from 0 to 9, with 0 being hottest and 9 being coolest. The mass of an M star can therefore vary over a range of $M_\star \approx (0.08 - 0.6)M_\odot$, with $M_\odot$ being the solar mass (M. J. Pecaut & E. E. Mamajek 2013). Given that we aim to simulate Earth-like scenarios, we choose the instellation received by the modeled exoplanet to be equal to the insolation that Earth receives. The instellation $S_\star$, in terms of the solar constant $S_\odot$, received from the host star is given by

$$S_\star = \frac{L_\star}{{r_{p,\star}}^2}, \tag{1}$$

with $L_\star$ the luminosity of the host star in solar units ($L_\odot$) and $r_{p,\star}$ the planetary orbital radius in au units. The luminosity and the mass of a main-sequence star are linked by the traditional

luminosity–mass relationship that is often parameterized (M. Harwit 1998) as

$$L_\star = {M_\star}^{3.5}. \quad (2)$$

Combining Equations (1) and (2) allows us to determine the distance between the exoplanet and its host star

$$r_{p,\star} = \sqrt{\frac{{M_\star}^{3.5}}{S_\star}}. \quad (3)$$

By requiring $S_\star = S_\odot$, and by substituting the values of the M star mass, we obtain

$$r_{p,\star} \approx (0.01 - 0.4)\sqrt{\frac{{M_\odot}^{3.5}}{S_\odot}} = (0.01 - 0.4)\ \text{au}. \quad (4)$$

According to equilibrium tide theory, we can express the maximum potential height of the tidal bulge raised on the planetary surface by the star (C. D. Murray & S. F. Dermott 1999) as

$$h_{p,\star,\max} = \frac{M_\star}{m_p}\left(\frac{R_p}{r_{p,\star}}\right)^3 R_p, \quad (5)$$

where R_p is the planetary radius and m_p is the mass of the planet. Therefore, by using the aforementioned stellar mass limits and the range of values of the planetary orbital radius obtained in Equation (4), the maximum theoretical height of the tidal bulge in the scenario of an Earth-mass planet orbiting an M star would be

$$h_{p,\star,\max} \approx (80000 - 9)h_{\oplus,\odot,\max}, \quad (6)$$

where $h_{\oplus,\odot,\max} \simeq 16$ cm is the maximum potential height of the equilibrium tide raised on Earth by the Sun.

We assume that the tidal potential energy, given by (C. D. Murray & S. F. Dermott 1999)

$$V = h_{p,\star}\frac{Gm_p}{{R_p}^2}, \quad (7)$$

where G is the gravitational constant, is completely transferred into kinetic energy, meaning that the maximum energy flux from ocean tides to vertical mixing (through bottom friction, internal wave generation and breaking, etc.) is proportional to $h_{p,\star,\max}$. Following the assumption that there is a linear relation between the vertical diffusion coefficient κ and said energy flux (Y. Si et al. 2022), we can estimate the magnitude of κ, which is therefore proportional to $h_{p,\star,\max}$. For instance, let us consider an example case of an M5 star with $M_\star = 0.21M_\odot$ (M. J. Heath et al. 1999), then $r_{p,\star} \approx 0.07$ au, and therefore $h_{p,\star,\max} \approx 800h_{\oplus,\odot,\max}$.

Given the average estimate for Earth $\kappa_\oplus = 1 \times 10^{-4}\ \text{m}^2\ \text{s}^{-1}$ (W. Munk & C. Wunsch 1998), we let the value of the globally uniform vertical diffusion coefficient vary within a range $\kappa = (0.5\text{–}5000)\kappa_\oplus = 0.5, 1.5, 5.0, 15, 50, 150, 500, 1500, 5000 \times 10^{-4}\ \text{m}^2\ \text{s}^{-1}$ and carry out climatic simulations adopting these values. The low limit of this range of values corresponds to a vertical diffusion coefficient that is lower than Earth's and a scenario characterized by especially weak tidal forcings. The upper limit would, in the case of a planet orbiting a low-mass star, correspond to a host star mass of approximately $0.13M_\odot$.

2.3. Planet Configuration

Given that planetary climates are deeply impacted by the arrangement of land and ocean topography, the choice of planetary topography is particularly important (E. Macdonald et al. 2022). In principle, an infinite number of continental configurations are possible for a terrestrial planet. Even though the possibility of extensively exploring realistic synthetic topographies of rocky exoplanetary bodies (F. Landais et al. 2019) is interesting, it is also very time consuming. Through investigating a limited number of simple configurations, it is however possible to draw valid conclusions regarding planetary climate and to evaluate potential habitability in different scenarios.

For instance, when dealing with idealized climate models that consider the contribution of the ocean, two categories of land configurations are often adopted: the pure aquaplanet and the ridgeworld (for example R. S. Smith et al. 2006, D. Ferreira et al. 2010, J. Yang et al. 2019, S. J. van de Velde et al. 2021). In the first case, the ocean covers the entire globe and no topographic constraints are present. Here, large zonal ocean currents can dominate, particularly at the equator. In addition, the zonal pressure gradients that can support a planetary scale overturning circulation are largely absent. In the second case, a number of strips of land extend in the meridional direction obstructing ocean flows and can feature gaps at different latitudes. Such configurations are chosen as they provide simple representations of how ocean circulation can vary according to different more specific topographic configurations that include multiple continents distributed at different positions across the globe.

In this study, we consider an Earth-sized planet characterized by preindustrial atmospheric concentrations of CO_2, covered by a single, global-scale ocean basin of uniform depth (5500 m) with limited and idealized hemispherically symmetric expanses of land. The land mass is characterized by two polar islands that extend to 86°N/S, which prevent eventual numerical instabilities resulting from grid convergence to arise. The chosen configuration features a single, 2° wide meridional ridge 145 m below the surface that connects the two polar islands and allows an overturning circulation.

2.4. System Architecture

We assume that the orbital and dynamical characteristics of the system (orbital semimajor axis, orbital eccentricity, planetary rotation period, planetary axial tilt, planetary mass, atmospheric composition) are the same as for the Earth–Sun system.

We adopt a solar spectral energy distribution, and we assume an Earth-like stellar radiation forcing at the top of the atmosphere: $S_\odot = 1365\ \text{W m}^{-2}$. Once the simulated climates reach a quasi-steady state after 2000 yr, the instellation value is reduced to a fraction of the solar constant (0.90, 0.85, $0.80S_\odot$), and we let the simulations run until a new steady climate state is reached.

3. Results

3.1. Effect of Vertical Diffusion: Circulation and Temperature Structure

The ocean meridional circulation is tightly linked to the value of κ. The Atlantic Meridional Overturning Circulation (AMOC) on Earth (M. W. Buckley & J. Marshall 2016) is a particularly interesting analog of the Aquaplanet Meridional Overturning Circulation (AQMOC).

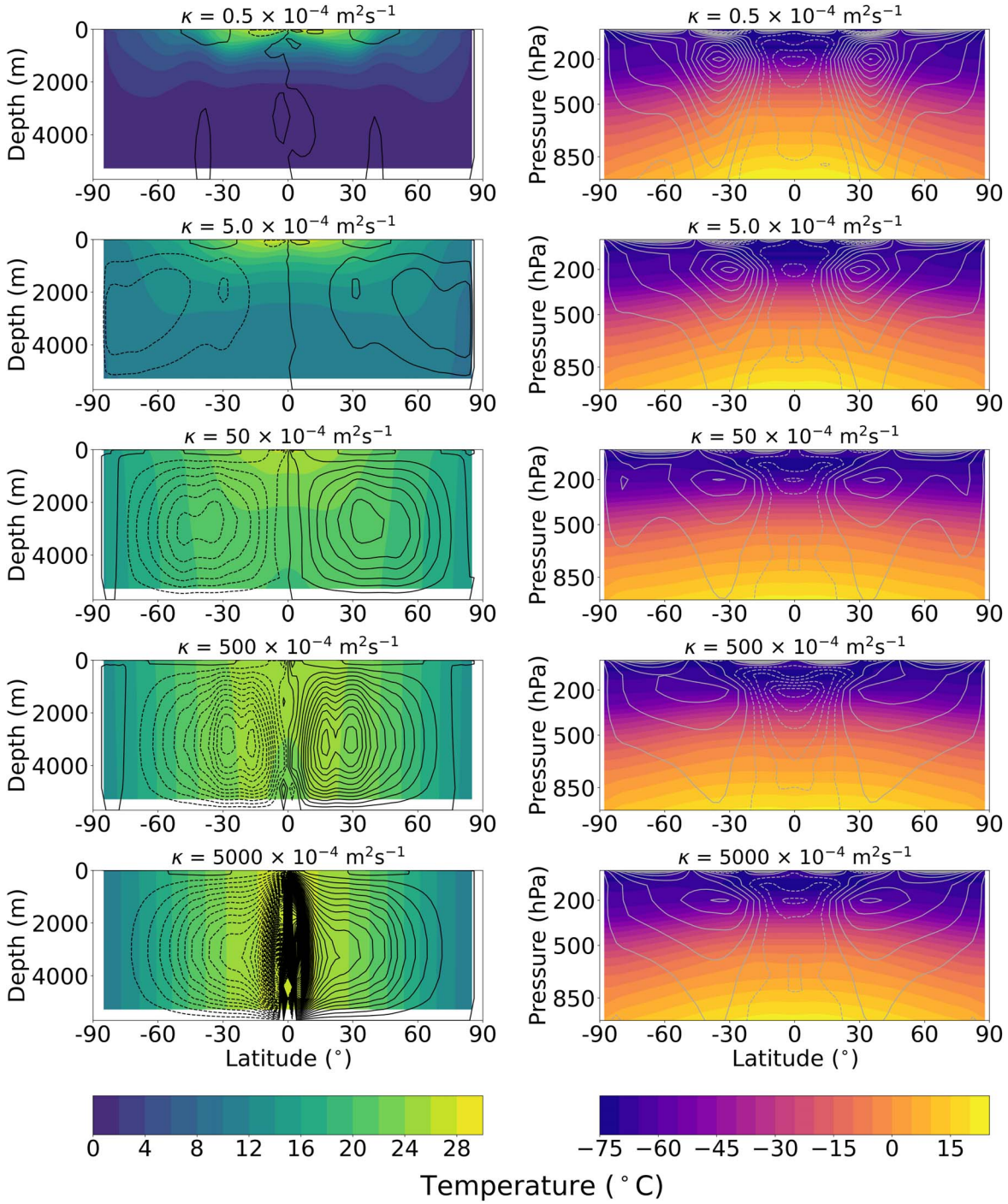

Figure 1. Shading shows zonally averaged values of temperature for the ocean (left) and the atmosphere (right). Black contours show the meridional overturning streamfunction. Contour interval is 50 Sv. Clockwise circulation is depicted by solid lines; counterclockwise circulation is depicted by dashed lines. Gray contours show the zonal wind. Contour interval is 3 m s^{-1}. Westerlies are depicted by solid lines; easterlies are depicted by dashed lines. Quantities are averaged over the last simulated 100 yr for each case.

The mechanisms driving the thermohaline currents that form this conceptual conveyor belt (W. S. Broecker 1991) are the same as those on Earth. Here, this overturning circulation is of fundamental importance to establish the climate we experience today, since it distributes heat and salt around the globe and carries nutrients necessary to sustain biological activities and support ocean life (M. W. Buckley & J. Marshall 2016). Essentially, warm surface water near the equator moves northward, gradually losing heat to the atmosphere. Colder water is denser, especially if subjected to sea ice formation processes, since salt is left behind in the ocean water. Toward the poles water sinks, and flows equatorward at depth. Eventually, the circulation is completed with a process called upwelling, when the water that has reached lower latitudes (or the Southern Ocean in the case of present-day Earth) is pulled toward the surface, and then proceeds to warm and start the cycle again.

The left panel of Figure 1 shows the zonally averaged ocean temperature (shading) and the overturning streamfunction

(black contours) as a function of depth and latitude for each of the analyzed cases. In every figure, circulation cells exist that move water in a clockwise (counterclockwise) motion in the northern (southern) hemisphere, from the equator to higher latitudes at surface and in the opposite direction at depth. While the topographic configuration in every case is hemispherically symmetric, a few slight differences appear between the two hemispheres for both quantities shown here, because of the adoption of Earth's orbital characteristics, i.e., the planet is located at the orbit's periapsis during northern winter/southern summer and at the apoapsis during northern summer/southern winter.

In general, the results show hemispheric AQMOC cells that envelope the whole planet, different from what happens on present-day Earth (the AMOC). Increasing values of κ result in an enhanced circulation, which is evident by an increasing number of black contours in Figure 1. As oceanic diffusion increases, the thermocline deepens progressively, and deep water at depths below 1–2 km becomes warmer, especially at low latitudes.

As κ increases and more efficient circulation (and thus redistribution of heat) is achieved, temperature minima increase and temperature maxima decrease, resulting in a flattening of the meridional surface temperature profile. When a threshold value of $\kappa \approx 150\text{–}500 \times 10^{-4}\,m^2\,s^{-1}$ is reached, the opposite behavior arises: for higher vertical diffusivities, the overturning cells become confined to lower latitudes, and water is effectively mixed in the vertical, but less efficiently moved in the meridional direction.

Sea surface temperature variations with κ have an impact on the atmosphere. The right panel of Figure 1 shows the zonally averaged atmospheric temperature and zonal winds for each of the analyzed cases. Subtropical jet streams are more intense for lower values of κ, associated with a larger meridional gradient in surface temperature, and become progressively less intense as κ increases and the meridional temperature profile is flattened, as shown by the decreasing number of gray contours. This trend is reversed once the threshold value of κ is reached, and the differences between equatorial and polar temperatures become starker.

In association with the gradual flattening of the meridional surface temperature gradient as κ increases, the Intertropical Convergence Zone becomes less defined in shape. Figure 2 shows how rainfall bands, distinctly separated in the low-κ scenarios, progressively weaken, broaden, and merge as κ increases.

Figure 1 shows, both for the ocean and the atmosphere, a behavior that is qualitatively similar to the one presented in Y. Si et al. (2022; temperature shown in Section 3.3 and circulation shown in Figure 1) for similar values of κ. Noticeable asymmetries, especially for the ocean, are due to the fact that the adopted topography presents Earth-like continents. Relying on these results to infer a trend from for high values of κ would however be misleading, as nonlinearities arise for $\kappa > 100 \times 10^{-4}\,m^2\,s^{-1}$.

3.2. Effect of Vertical Diffusion: Ocean Temperature and Heat Transport

The total poleward heat transport (combined atmospheric and oceanic components) at 35°N increases from 4.46 to 5.69 PW as κ increases from 0.5×10^{-4} to $500 \times 10^{-4}\,m^2\,s^{-1}$, and then slowly decreases for even higher values of κ

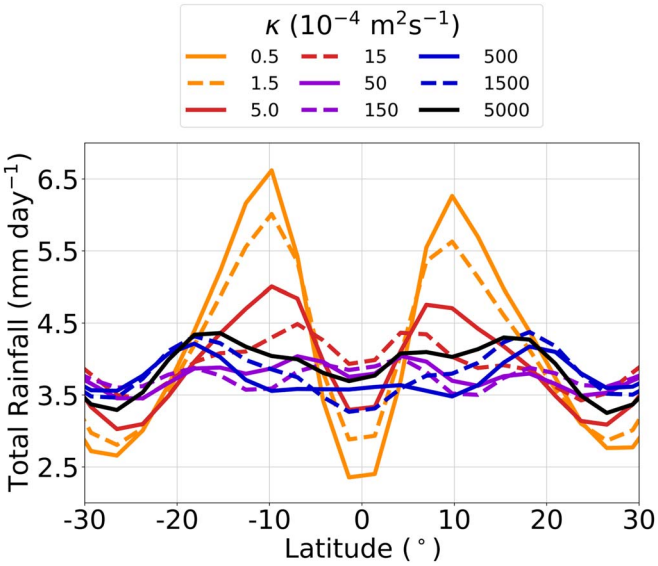

Figure 2. Zonal mean of the total rainfall as a function of latitude and κ. Quantities are averaged over the last 100 yr for each simulation.

(Figure 3(c)). While the maximum value of the total heat transport is reached around 35–40°N for each value of κ, it is interesting to note that the ocean heat transport peaks at low latitudes for low values of vertical diffusion, starting from about 9°N for $\kappa = 0.5 \times 10^{-4}\,m^2\,s^{-1}$, and then shifts toward higher latitudes, settling at about 30°N for higher values of κ.

Although the total heat transport varies within a small range as κ varies, the changes in oceanic and atmospheric heat transport are much larger with a degree of compensation between these components. Low oceanic heat transport at low values of κ results in a higher atmospheric heat transport and conversely high oceanic heat transport at high values of κ results in a lower atmospheric heat transport.

Heat transport in the ocean is mainly carried out through two different circulation processes: the AQMOC and the horizontal gyres. Figure 3(d) shows the total advective ocean heat transport and its components due to the AQMOC and the gyre circulation, computed with monthly averaged data. Unlike the oceanic heat transport shown in Figure 3(c), the advective part of oceanic heat transport in Figure 3(d) does not take into account submonthly transient effects and diffusion processes. As a result of the particularly efficient mixing associated with high values of κ, the temperature gradient between the top and the bottom layers of the ocean becomes progressively smaller, and vertical stratification disappears (Figures 1 and 3(a)). In this scenario, the heat transport associated with the gyre circulation becomes more important than the overturning component, as the vertical temperature gradient is eroded but the horizontal gradient remains.

Higher values of κ correspond to a more efficient oceanic vertical mixing, which consequently means that as the surface to ocean bottom temperature gradients decrease, the volume-averaged temperatures steadily increase (Figure 4). Meridional gradients of surface temperature reach a minimum between $\kappa \sim 150\text{–}500 \times 10^{-4}\,m^2\,s^{-1}$, which corresponds to the peak in heat transport.

For comparison, the three values of the vertical diffusion coefficient adopted by Y. Si et al. (2022) are $\kappa = 1, 10, 100$ and $\kappa_{\oplus} = 1,\ 10,\ 100 \times 10^{-4}\,m^2\,s^{-1}$ (see Figure 3). The behavior shown in Figure 3(c) is qualitatively comparable to that

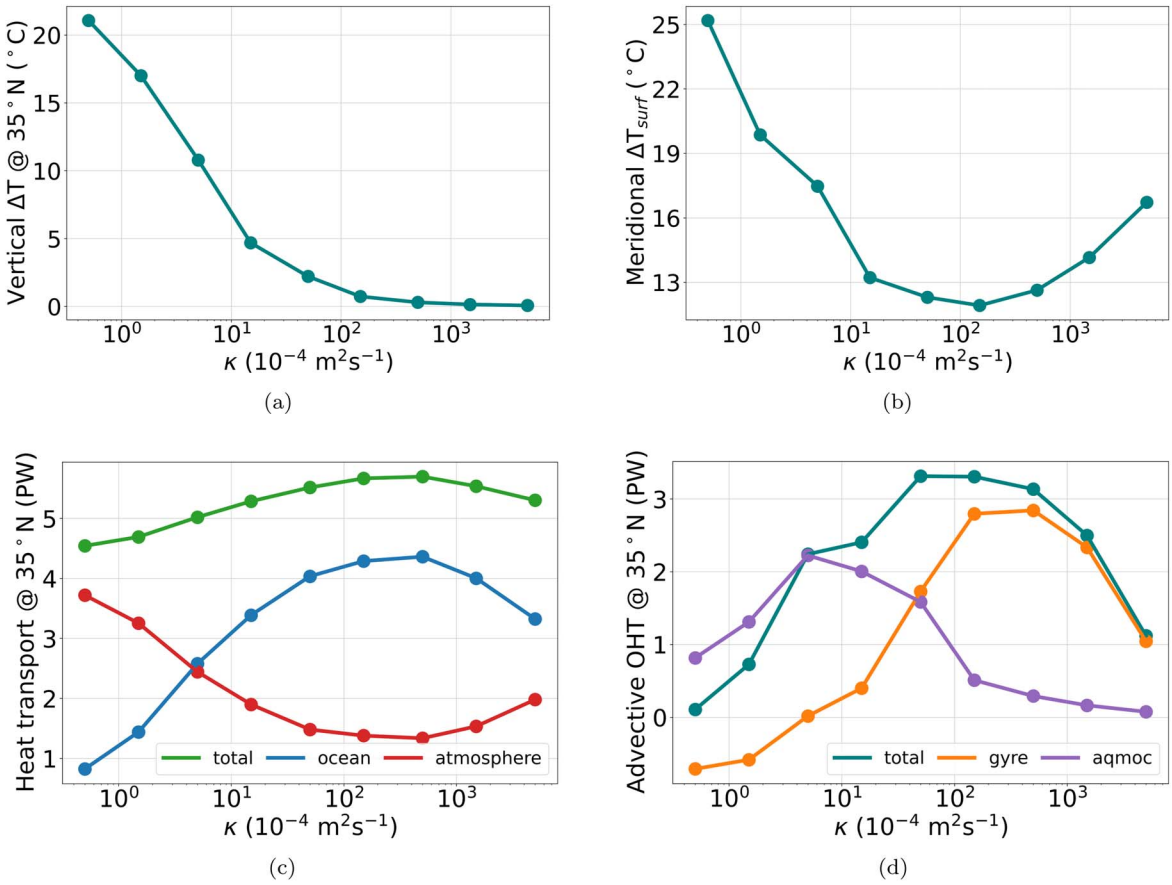

Figure 3. Mean climatic properties as a function of κ. Quantities are averaged over the last 100 yr for each simulation. (a) Zonal mean vertical temperature difference (surface–bottom) at 35°N; (b) zonal mean meridional surface temperature difference (equator–pole); (c) total, ocean, and atmosphere meridional heat transport at 35°N; (d) advective components of the meridional ocean heat transport at 35°N.

$S_\star$ ($S_\odot$)	κ (10^{-4} m^{2}s^{-1})	Mean annual climate state		
		T_{surf} (°C)	T_{vol} (°C)	ϕ_{ice} (° N/S)
1.00	0.5	**20.6**	**3.7**	**86.0**
	5.0	**21.6**	**13.0**	**86.0**
	50	**22.3**	**20.5**	**86.0**
	500	**22.1**	**22.1**	**86.0**
	5000	**21.9**	**22.2**	**86.0**
0.90	0.5	*6.6*	*-0.0*	*39.0*
	5.0	**14.8**	**7.0**	**86.0**
	50	**15.3**	**13.7**	**86.0**
	500	**15.5**	**15.5**	**86.0**
	5000	**15.0**	**15.3**	**86.0**
0.85	0.5	***-2.2***	***-1.9***	***0.0***
	5.0	***-2.2***	***-1.9***	***0.0***
	50	**10.7**	**9.3**	**86.0**
	500	**11.1**	**11.2**	**86.0**
	5000	**10.4**	**10.7**	**86.0**
0.80	0.5	***-2.2***	***-1.8***	***0.0***
	5.0	***-2.2***	***-1.9***	***0.0***
	50	***-2.2***	***-1.9***	***0.0***
	500	*4.1*	*4.2*	*51.2*
	5000	***-2.2***	***-1.9***	***0.0***

Figure 4. Values of sea surface temperature, volume-averaged oceanic temperature and latitude reached by sea ice corresponding to different values of instellation and κ. The values represent the mean annual climate state and are computed at the end of each simulation, once the climate is considered stable, and averaged over 10 yr. bold values indicate planets that may not form any sea at all, italic values indicate planets with a surface that might be partially covered by some ice, and bold–italic values indicate planets that may eventually become frozen.

presented in Figure 3 of Y. Si et al. (2022), with increasing ocean heat transport and decreasing atmosphere heat transport as κ increases. The main differences in our results for similar values of κ consist in the latitude of the peak in heat transport and in overall lower values of heat transport, both ascribable to a different planetary configuration. Once again, taking into consideration higher values of κ allows us to unveil a nonmonotonic trend that would otherwise remain undetected.

3.3. Effect of Change in Instellation

Ocean diffusion plays an important role in determining the basic state of the planetary surface, and therefore in determining quantities that are tightly linked to the concept of habitability, such as surface temperatures. For instance, a low value of κ implies that less heat is transported away from the warmest regions at low latitudes and toward the coldest regions at high latitudes, increasing the temperature of the warmest regions and further cooling down the coldest regions—such a situation implies that an ocean with a low value of κ will completely freeze over at values of instellation that can support a non-frozen ocean with a higher value of κ.

In order to test the impact that ocean tidal mixing might have on the position of the outer edge of the habitable zone, we run a set of simulations with a reduced instellation ($S_\star = 0.90$, 0.85, $0.80 S_\odot$) for the cases $\kappa = 0.5$, 5.0, 50, 500, 5000 $\times$ 10^{-4} m^2 s^{-1}. The new simulations are started from the steady climate state reached in the case of $S_\star = S_\odot$, and are run until a new equilibrium state was achieved. A reduced instellation

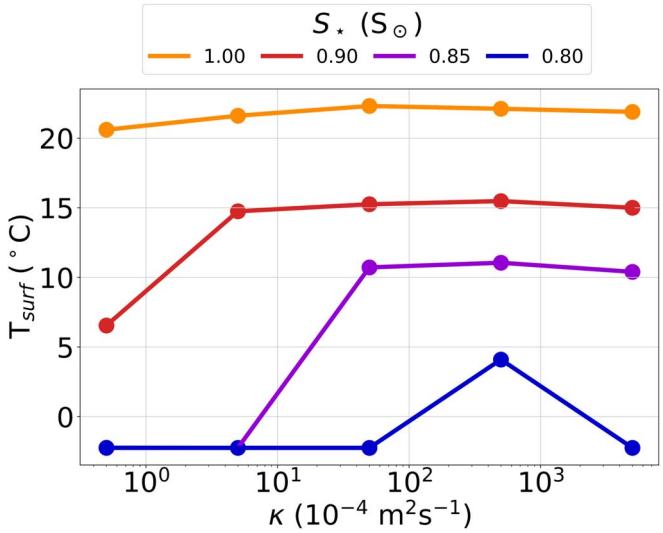

Figure 5. Globally averaged surface temperature as a function of κ for different values of instellation. Quantities are averaged over the last 10 yr for each simulation.

causes a drop in temperatures and, in some cases, the formation of sea ice. A more efficient oceanic heat transport mitigates these effects. In some scenarios, the planets characterized by higher values of κ are spared from completely freezing over. An enhanced oceanic circulation can prevent the planet from freezing over. On the contrary, an inefficient heat redistribution can be associated with a quick global glaciation: once sea ice starts forming at high latitudes, a strong ice-albedo feedback causes its rapid expansion toward lower latitudes.

The results summarized in Figure 4 and Figure 5 show a variety of scenarios: planets receiving the same amount of energy from their host star, but characterized by different values of κ, may eventually become completely frozen (Figure 4, bold–italic values), their surface might be partially covered by some ice (italic values), or they might not form any sea ice at all (bold values). In general, values of κ associated with efficient heat transport (see Figure 3(c)) result in warmer climates. More specifically, if we focus on the case $S_\star = 0.80 S_\odot$, the scenario characterized by $\kappa = 500 \times 10^{-4}\,\mathrm{m^2\,s^{-1}}$, associated with the peak in heat transport discussed in the previous section, is the only case in which the planet is not completely frozen, but rather features sea ice that extends from the poles to $\sim 50^\circ$N/S. These results demonstrate that the variation of tidal strength has an impact not just on climate, but also habitability in a nonmonotonic manner.

Ocean diffusion effectively plays a role in determining the position of the outer edge of the habitable zone, which presents an outward shift in the scenarios characterized by efficient meridional heat transport. Referring to Equation (3), a 20% decrease in instellation corresponds roughly to a 12% increase of the orbital radius of the habitable zone.

4. Discussion and Conclusions

In this Letter we address the issue of estimating the impact of ocean tides on planetary climate, in the case of a water-rich planet residing in the habitable zone of a low-mass star.

We demonstrate that enhancing tidally driven vertically diffusivity in the ocean crucially influences the global circulation patterns and the strength of overturning cells in a "ridgeworld" climate model, and dictates the amount of heat transported meridionally, therefore playing an important role in determining the temperature of the planetary surface. Concurrently, tidal energy dissipation has an impact on other quantities that characterize the planetary surface. For instance, given the strong interaction between the ocean and the atmosphere, lower values of κ result in larger latitudinal gradients of surface temperature, therefore resulting in more intense zonal winds.

The magnitude of κ has significant implications for the mechanisms at play in transporting heat in the ocean. Our findings suggest that a more efficient vertical diffusion, and the consequent reduction of vertical stratification, enables the horizontal gyres to become the predominant medium to transport heat.

Interestingly, the results point to a nonlinear and nonmonotonic effect of the vertical diffusion coefficient on several climatic variables. Having expanded the range of values of diffusivity previously considered (Y. Si et al. 2022), here we argue for the existence of a threshold value of κ at which surface temperature and oceanic heat transport are maximized (see Figure 3(c)).

The effect of tidal mixing on climate is especially noteworthy if it is possible to distinguish different scenarios from observed surface features. In the case of reduced instellation, ice coverage of the planetary surface would be an especially effective observable. We find that, for a fixed instellation value (for example $S_\star = 0.85 S_\odot$), sea ice changes from covering the entirety of the planetary surface to being completely absent depending on the choice of κ. In the case of a solar instellation, $S_\star = S_\odot$, cloud patterns could offer an insight into the climate dynamics of the observed planet. We find that planets characterized by different κ present different Intertropical Convergence Zone configurations, consistent with the surface temperature profile depicted in Figure 1. For low values of κ, the Intertropical Convergence Zone appears to be split in two bands separated by an evident equatorial cold tongue, and these two bands merge into a singular band across the equator as κ increases. This effect is seen on a regional scale, and therefore is not observable with the present technology that can at best characterize surface properties of exoplanets on a global scale. Advances in observational technologies might unveil such characteristics in the near future.

This study aims at highlighting how the climates of planets affected by significant tidal forces differ from the reference case of the Earth. Our simulations are based on several assumptions. We choose to simulate the case of a water-rich planet characterized by a simple ridgeworld configuration and we focus on parameterizing the impact of ocean tides. We assume that our results are general enough for the case of any planet with oceans that features some kind of meridional barrier. To validate this statement, we run simulations where the pole-to-pole grid cell wide ridge is split into multiple sections spread over a range of longitudes. We find that the results from these runs do not present significant differences from the standard scenario analyzed in this Letter.

We do not take into account the different nature of the stellar spectrum of a low-mass star compared to the solar equivalent, nor do we factor in the effect of the host star spectral energy distribution on the ice-albedo feedback (in this study, the adopted ice albedo is 0.6). For instance, A. L. Shields et al. (2013)

conducted a study regarding the ice latitude of exoplanets orbiting three different types of host stars, varying the amount of instellation and taking into account the wavelength-dependent reflectivity of ice and snow. Using CCSM4, they found that an M dwarf planet entered a snowball state at $S_\star = 0.73S_\odot$, compared to the instellation value necessary for a planet orbiting a G star to completely freeze over, that is, $S_\star = 0.92S_\odot$.

Even though the adopted model is different from FORTE2.0, we can safely assume that we would obtain a similar outcome in our case, which would mean that the outer edge of the habitable zone would be further outwardly shifted if we considered the ice and snow albedos to be lower for a host star colder than the Sun. Similarly, different levels of CO_2 would change the value of $S_\star$ at which the formation of sea ice, and ultimately global glaciation, occur.

An additional factor that is not taken into account in this study is the contribution of planetary tidal heating, which could provide an additional source of heat. Including this aspect of the tidal forcings exerted on the simulated planet would once again temper the onset of snowball scenarios and further extend the outer edge of the habitable zone. The above effects, as well as the cases of planetary rotation rates dissimilar to the Earth's, and specifically spin–orbit resonances, are topics that are left for future work.

In conclusion, we show how a nonlinear and nonmonotonic relationship exists between ocean circulation, climate, potential habitable zone width, and ocean tidal mixing κ. The potential habitability of asynchronously rotating tidally locked planets implicitly depends on the stellar type through the effect of stellar size on star–planet distance and ocean tidal strength, and hence κ. Our results apply to any case in which a terrestrial planet is subjected to strong nonstationary tidal forcings, which include those being orbited by either massive or close satellites. For example, on Earth the equilibrium lunar tide is more than twice as strong as the equilibrium solar tide. An appropriate choice of κ, associated with enhanced oceanic heat transport, can lead to planets being spared from entering a snowball state and completely freezing over, or equivalently to an outward shift of the outer edge of the habitable zone, effectively widening the circumstellar region that can host potentially habitable planets.

Acknowledgments

This work was supported by the Engineering and Physical Sciences Research Council (grant No. EP/W524074/1). The research presented in this Letter was carried out on the high-performance computing cluster supported by the Research and Specialist Computing Support service at the University of East Anglia. M.D.P., D.S., and M.J. conceived the study. M.D.P. conducted the experiments. All authors contributed to the analysis. All authors reviewed the manuscript.

Data Availability

The FORTE2.0 A. T. Blaker et al. (2021) code, compilation instructions, and example run scripts, together with all necessary ancillary files, are accessible via A. Blaker et al. (2020).

The data that support the findings of this study are accessible via doi:10.5281/zenodo.13961191.

ORCID iDs

Maria Di Paolo https://orcid.org/0000-0002-0735-2557
David P. Stevens https://orcid.org/0000-0002-7283-4405
Manoj Joshi https://orcid.org/0000-0002-2948-2811
Rob A. Hall https://orcid.org/0000-0002-3665-6322

References

Barnes, R. 2017, CeMDA, 129, 509
Blaker, A., Joshi, M., Sinha, B., et al. 2020, NOC-MSM/FORTE2.0: FORTE 2.0: A Fast, Parallel and Flexible Coupled Climate Model, v2.0.1, Zenodo, doi:10.5281/zenodo.4108373
Blaker, A. T., Joshi, M., Sinha, B., et al. 2021, GMD, 14, 275
Broecker, W. S. 1991, Ocgpy, 4, 79
Bryan, F. 1987, JPO, 17, 970
Buckley, M. W., & Marshall, J. 2016, RvGeo, 54, 5
Correia, A. C. M., & Laskar, J. 2004, Natur, 429, 848
Cullum, J., Stevens, D., & Joshi, M. 2014, AsBio, 14, 645
Cullum, J., Stevens, D. P., & Joshi, M. 2016, PNAS, 113, 4278
Del Genio, A. D., Way, M. J., Amundsen, D. S., et al. 2019, AsBio, 19, 99
Dobrovolskis, A. R., & Ingersoll, A. P. 1980, Icar, 41, 1
Ferreira, D., Marshall, J., & Campin, J.-M. 2010, JCli, 23, 1456
Ferreira, D., Marshall, J., O'Gorman, P. A., & Seager, S. 2014, Icar, 243, 236
Harwit, M. 1998, Astrophysical Concepts (Berlin: Springer), 290
Heath, M. J., Doyle, L. R., Joshi, M. M., & Haberle, R. M. 1999, OLEB, 29, 405
Hu, Y., & Yang, J. 2014, PNAS, 111, 629
Joshi, M., Stringer, M., van der Wiel, K., O'Callaghan, A., & Fueglistaler, S. 2015, GMD, 8, 1157
Kilic, C., Lunkeit, F., Raible, C. C., & Stocker, T. F. 2018, ApJ, 864, 106
Landais, F., Schmidt, F., & Lovejoy, S. 2019, MNRAS, 484, 787
Leconte, J., Wu, H., Menou, K., & Murray, N. 2015, Sci, 347, 632
Macdonald, E., Paradise, A., Menou, K., & Lee, C. 2022, MNRAS, 513, 2761
Munk, W., & Wunsch, C. 1998, DSRI, 45, 1977
Murray, C. D., & Dermott, S. F. 1999, Solar System Dynamics (Cambridge: Cambridge Univ. Press), 130
Musgrave, R., Pollmann, F., Kelly, S., & Nikurashin, M. 2022, Ocean Mixing: Drivers, Mechanisms and Impacts (Amsterdam: Elsevier), 117
Olson, S. L., Jansen, M., & Abbot, D. S. 2020, ApJ, 895, 19
Pecaut, M. J., & Mamajek, E. E. 2013, ApJS, 208, 9
Read, P. L. 2014, AsBio, 14, 627
Shields, A. L., Ballard, S., & Johnson, J. A. 2016, PhR, 663, 1
Shields, A. L., Meadows, V. S., Bitz, C. M., et al. 2013, AsBio, 13, 715
Si, Y., Yang, J., & Liu, Y. 2022, A&A, 658, A33
Smith, R. S., Dubois, C., & Marotzke, J. 2006, JCli, 19, 4719
Trenberth, K. E., & Caron, J. M. 2001, JCli, 14, 3433
Vallis, G. K., & Farneti, R. 2009, QJRMS, 135, 1643
van de Velde, S. J., Hülse, D., Reinhard, C. T., & Ridgwell, A. 2021, GMD, 14, 2713
Webb, D. J. 1996, CG, 22, 569
Winton, M. 2003, JCli, 16, 2875
Yang, J., Abbot, D. S., Koll, D. D. B., Hu, Y., & Showman, A. P. 2019, ApJ, 871, 29